"Novel Drilling Technology Combining Hydro-Jet and Percussion for ROP Improvement in deep geothermal drilling"

This project has received funding from the European Union's Horizon 2020 research and innovation programme under grant agreement No 101006752

DELIVERABLE 5.4

"Report on numerical modelling of groove jetting, jettability and optimisation"

ABSTRACT

The ORCHYD project's hybrid technology relies on creating a deep groove with a HPWJ, aiming for ~ 20 mm depth. This groove modification reduces rock resistance to a rotating drill's percussive hammering. Our goal is to develop a predictive model for maximising groove depth under challenging deep geothermal conditions, beyond the capabilities of laboratory drilling test rigs.

We outline methods for characterising coarse-grained granite (Sidobre Silverstar) and calibrating a combined finite-discrete element (FDEM) model for jet grooving. Validation uses ARMINES' benchmark data from Pau Labs, simulating non-traversing jets within a microstructure-based domain (~20 mm) for less than 1 second. Advanced techniques inform the granite's characterisation, integrating micro-mechanical properties. We modify the Solidity FDEM code for realistic pressure conditions and enable new fracture surface generation using spatially and temporally varying pressure boundaries.

We introduce an innovative calibration process using a 10 mm Brazilian disc experiment, nano-indentation testing, and machine learning for parameter calibration. An adjustable Defect Intensity (DI) parameter, set at 30%, closely matches simulation and benchmark conditions: 1 mm nozzle, 240 MPa jet chamber pressure, and 20 MPa back and confining pressure. Our models reveal granite's heterogeneity in response to local jetting, showcasing a spectrum of responses influencing groove or crater depths. These variations depend on the jet's starting point, crystalline topology, and mineral phases, leading to differing outcomes.

The validated model was applied to a traversing nozzle scenario at 157 mm/s. Results from a few simulations and experiments consistently showed groove depths between 4-6 mm, suggesting an optimal speed for depth maximisation. In the next phase, the model will investigate jetting under realistic, anisotropic stress conditions for geothermal resources at depths of 4-5 km.

DOCUMENT TYPE	Report
DOCUMENT NAME:	Deliverable D5.4.
VERSION:	vfinal
DATE:	05 Dec 2023
STATUS:	S0
DISSEMINATION LEVEL:	PU

AUTHORS, REVIEWERS				
AUTHOR(S):	John-Paul Latham, Jiansheng Xiang, Sadjad Naderi			
AFFILIATION(S):	Imperial College London			
FURTHER AUTHORS:				
PEER REVIEWERS:	Laurent Gerbaud, Hedi Sellami, Naveen Velmurugan, Alexandre Kane			
REVIEW APPROVAL:	Approved	Yes	Rejected (to be improved as indicated below)	No
REMARKS / IMPROVEMENTS:				

VERSION HISTORY			
VERSION:	DATE:	COMMENTS, CHANGES, STATUS:	PERSON(S) / ORGANISATION SHORT NAME:
V0.1	09/10/23	First draft	John-Paul/ ICL
V1.1	25/11/23	Version after all reviews	John-Paul/ ICL
VFINAL	05/12/23	Final version to submit	Naveen/ ARMINES

VERSION NUMBERING	
v0.x	draft before peer-review approval
v1.x	After the first review
v2.x	After the second review
vfinal	Deliverable ready to be submitted!

STATUS / DISSEMINATION LEVEL			
STATUS		DISSEMINATION LEVEL	
S0	Approved/Released/Ready to be submitted	**PU**	Public
S1	Reviewed	**CO**	Confidential, restricted under conditions set out in the Grant Agreement
S2	Pending for review		
S3	Draft for comments	**CI**	Classified, information as referred to in Commission Decision 2001/844/EC.
S4	Under preparation		

TABLE OF CONTENTS

CONTENT

1 Introduction

1.1 Context and Scope

In WP5 the HPWJ Grooving Process is studied. The key tasks of WP5 as set out in the proposal (see **Figure 1**) were discussed in the introduction to the report D5.1.

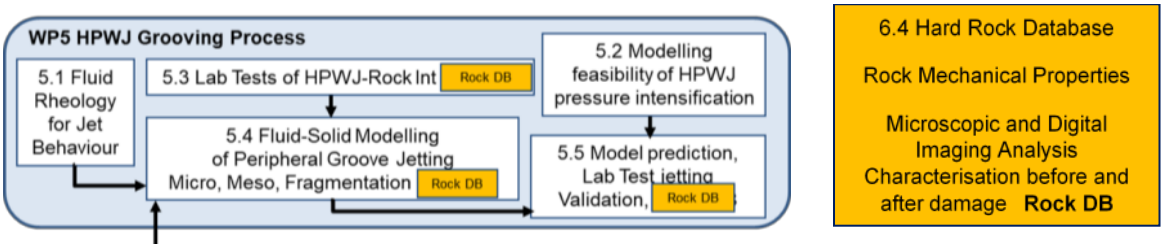

Figure 1: Structure of WP5 as in the original proposal. Work packages involving assessment of the hard rock suite to be considered are identified as the rock database assembled under WP6, Task 6.4.

The original titles of Tasks 5.4 "*numerical modelling of the rock destruction processes during kerf groove cutting*" and Task 5.5 "*groove-cutting optimisation – synthesis of numerical and experimental results*", were recognised to have an overlap which led to the tasks and deliverables being rationalised during the early phase of the ORCHYD project. It was agreed to have Task 5.4 addressing development and validation of the microstructural-based model using experimental data from Task 5.3. Such a model would address destruction applicable to the rock in the small region of the jet's immediate influence – i.e., directly under the 1 mm diameter jet. Microstructural model development and its validation is the main subject of this renamed deliverable, D5.4. Because of the mineral grain scale, small elements and small time-steps are needed for accurate simulation. The jet-rock interaction microstructure-based model is only applied to the modelling of a small fraction (a few degrees) of a full 360-degree rotation of the bit, with the jet traversing a small arc. Beyond this limited range, the behaviour becomes repetitive and periodic, offering diminishing returns in terms of insights gained from simulating additional degrees. As it is very expensive to model spatial and temporal scales of interest for generalisation to steady-state drilling using such a microstructure-based model (i.e., the simulation runtimes are totally impractical), a mesoscale model giving groove cutting performance is also developed as this may prove more useful to evaluate HPWJ in the context of hybrid drilling.

The research leading to the development of an alternative numerical model of jetting at the mesoscale will be reported in D5.5. The aim of the work to be reported in D5.5 is to draw together the conclusions from experiments and numerical models on how to maximise the depth of groove based on the range of in-situ conditions and practical HPWJ settings. Calibrated HPWJ models are applied to illustrate effects due to rock type and their sensitivity to jetting conditions and in-situ conditions. In having such grooving models, we can then apply them in WP7 e.g., for conditions that cannot be created in experimental rigs in the laboratory. Before, embarking on the report details, it is important to highlight how the scope of this task has changed since the original proposal was written.

A two-way coupled numerical model of the jetting erosion of a sandstone rock was applied by ICL in previous EU projects [1], and it had been suggested that such an approach could be used again. However, in this research for ORCHYD, to create more reasonable run-times, the fluid model (CFD) is separated from the solid destruction model by applying the CFD model's velocity and pressure results. In this one-way coupled approach, a realistic pressure boundary condition associated with a given jet velocity, stand-off distance and jet orifice diameter can then be applied to a solid mechanics model over the surface area of jet impingement [2]. The details of the pressure boundary condition approach are given in this report.

In **Figure 1**, it is apparent that for the model calibration research intended for Tasks 5.3, 5.4 and 5.5, (and 6.1) not only would rock mechanical property data become available for those tasks, and to reside in a shared database, but also electron microscopic digital image analysis for characterisation of specimens before and after jetting damage was envisaged as part of the methodology to be employed for model calibration. Unfortunately, the characterisation part was not included in the initial project resourcing and planning. Therefore, such key data was not going to become available for use in good time for the modelling work in WP5 and WP6. Consequently, ORCHYD was faced with a problem which was solved by the design and implementation of a programme of additional experimental and numerical research, funded by the good-will and time of ICL labs and staff, and colleagues in Bristol University, but with little control on the timeframe for its completion. Therefore, in parallel, to fill a gap in ORCHYD, a direct microstructure-based rock representation for use in the FDEM mechanical model, focussing on one rock type, namely Sidobre granite, was built and calibrated using micro-scale mineral properties and at the scale to assess multi-mineral properties. Such a microstructure-based model would also be essential for the FDEM and FEM continuum modelling to be conducted in the percussive-hammer bit modelling of WP6.

Here, in D5.4 we focus on one rock type, the Sidobre granite. To keep this report concise, details of the microstructure-based model will be reported in a journal paper and just a summary will be included here.

1.2 Aims and Objectives

The task has a revised aim – to develop a microstructure-based numerical model of HPWJ erosion applicable to deep (4-5) km field drilling conditions.

The objectives are to:

i. Generate a microstructural model representation of one granite (i.e., Sidobre) for use in FDEM simulation of HPWJ (or impact by hammer bit inserts) and a novel calibration methodology to account for grain boundary and intra-grain properties.
ii. Implement modifications to the Solidity FDEM code to simulate jetting action with a pressure boundary condition approach.
iii. Design benchmark experiments for short duration jetting tests essential to calibrate the numerical model parameters in collaboration with ARMINES.
iv. Review benchmark test results and conduct a validation study comparing experiments and model results.
v. Apply the model to deep in-situ conditions that could not be undertaken in the laboratory drilling rig.

2 Methodology: FDEM Simulation of HPWJ using Solidity

2.1 Introduction to FDEM

In FDEM (i.e., also known as FEMDEM), the domain is treated as a multi-body system, with each discrete element further discretised into finite elements. FDEM analyses the discontinuum behaviour, such as multi-body interactions and contacts at fracture surfaces, while the continuum behaviour, including deformation and stress within discrete elements, is analysed using FEM. The intact material is initially modelled as a continuum using FEM, and after fracture initiation, a mix of continua and fractures is considered, with FEM remaining in the continua and DEM handling the interaction between discrete fracture surfaces using contact algorithms. Joint elements are assigned deformation and strength parameters, and their failure represents crack initiation. The stress increases elastically with joint aperture until reaching the strength threshold, followed by a nonlinear strain-softening stage. Transitioning from unbroken elasticity to a fully non-cohesive crack typically requires 3 to 4 joint elements. A Mohr-Coulomb criterion with a tension cut-off determines the shear strength based on the normal stress perpendicular to the shear direction. Additionally, the DEM formulation allows for handling large displacement problems efficiently.

The FDEM method, pioneered by [3] has been widely applied in a variety of engineering problems [4-6]. A full account of the 3D fracture model implemented in ***Solidity*** by Guo and Xiang in 2014 can be found in Gou's PhD Thesis and in shorter form in [7] with a mesh sensitivity study of ***Solidity*** FDEM presented in [8].

2.2 Governing Equations

For the structural dynamics, FDEM is used in our model. The finite discrete element method initially developed by [9] is specially designed for simulating rock mechanics problems and has great advantages in simulating rock deformation and failure [3, 10, 11]. It is capable of simulating the transition process of the intact rock to discrete parts. In the FDEM model, the intact rock is discretised into triangular elements in 2D or tetrahedra elements in 3D. The elements next to each other are connected with the so-called joint elements which have non-linear responses to the relative displacement between the elements. Once the relative displacement between the elements exceeds a certain criterion, the joint element between them is assumed to be broken. This will be in a specific mode (tensile or shear) according to the criteria satisfied. The interaction between the elements belonging to different fracture surfaces in a single body or external surfaces from multi-bodies are computed according to their overlap in space.

In the three-dimensional fracturing simulations, the domain is discretised by 4-node tetrahedral elements and 6-node joint elements. The motions of element nodes are governed by internal forces and external forces acting on them. The governing equation for every individual node is given as:

$$m_i \dot{\mathbf{v}}_i + \mathbf{f}_{int} = \mathbf{f}_{ext} \quad (1)$$

where m_i is the mass of node i, $\dot{\boldsymbol{V}}_i$ is the acceleration vector of node i, $\boldsymbol{f}_{int}$is the internal force vector of node i, $\boldsymbol{f}_{ext}$ is the external force vector of node i. In three-dimensional fracturing simulations, the internal force $\boldsymbol{f}_{int}$ is calculated from stresses of tetrahedral elements. In **Eq. (2)**, the external force $\boldsymbol{f}_{ext}$ including three parts is calculated as:

$$\mathbf{f}_{ext} = \mathbf{f}_{joint} + \mathbf{f}_{contact} + \mathbf{f}_{load} \quad (2)$$

where $\boldsymbol{f}_{joint}$ is the external force vector contributed by the deformation in joint elements $\boldsymbol{f}_{contact}$ is the external force vector contributed by the contact interaction, **Eq. (10)** which will be introduced later) including normal compression and sliding friction, $\boldsymbol{f}_{load}$ is the external force vector contributed by external loading, such as body force and surface traction.

2.3 Explicit Time Integration

A forward Euler method is used in the 3D fracturing simulations for explicit time integration. After the calculation of all the parts contributing to the nodal force in **Eq. (3)**, the unbalance force can be calculated as:

$$\mathbf{f}_{unbalance} = \mathbf{f}_{ext} - \mathbf{f}_{int} \quad (3)$$

Then the acceleration and velocity at nodes are calculated as:

$$\dot{\mathbf{v}}_t = \frac{\mathbf{f}_{ext} - \mathbf{f}_{int}}{m_i} \quad (4)$$

$$\mathbf{v}_{t+1} = \mathbf{v}_t + \dot{\mathbf{v}}_t \Delta t \quad (5)$$

where $\dot{\boldsymbol{V}}_i$ is the acceleration vector of node i at the current time-step t, $\boldsymbol{V}_t$ is the velocity vector of node i at the current time-step t, $\boldsymbol{V}_{t+1}$ is the velocity vector of node i at the next time-step $t+1$, $\boldsymbol{f}_{ext}$ is the external force vector for node i, $\boldsymbol{f}_{int}$ is the internal force vector for node i, m_i is the mass of node i, and Δt is the time-step. Based on the obtained velocity, the node coordinates can be updated:

$$\mathbf{x}_{t+1} = \mathbf{x}_t + \mathbf{v}_{t+1} \Delta t \quad (6)$$

where $\boldsymbol{X}_t$ is the coordinate vector of node i at the current time-step t, $\boldsymbol{X}_{t+1}$ is the coordinate vector of node i at the next time-step $t+1$.

The choice of time-step is important for the numerical stability of the three-dimensional fracturing simulations. A time-step corresponding to approximately one-tenth of the time required for the stress wave to travel through a tetrahedral element is used. Based on the speed of stress wave propagating in a solid rod, the time-step Δt is estimated as:

$$\Delta t = min\left(\frac{h}{10}\sqrt{\frac{\rho}{E}}, \frac{1}{10}\sqrt{\frac{m_e}{E}}\right) \quad (7)$$

where ρ is the density, E is the Young's modulus, and h is the average length of the edges of tetrahedral elements, m_e is the mass of the smallest element.

2.4 Contact Detection and Interaction in a Discontinuum Domain

Detection of contact in the discontinuum domain has two possible meanings: discrete bodies collide when they move towards each other, and the normal compression and frictional sliding between discrete fracture surfaces is occurring. It should be noted that the microscopic roughness of fracture surfaces is not considered here. Because the entire domain is discretised

by tetrahedral elements, the contact detection and interaction algorithms in the three-dimensional FDEM code works on a tetrahedral element basis, which means the detected contacting couples are couples of tetrahedral elements that are in contact, and the contact forces are distributed to the nodes of tetrahedral elements. The detailed algorithms in this section can be found in the literature given below, so only a brief introduction is given here.

The contact algorithms used in the 3D fracturing simulations include two parts: contact detection and contact interaction. In [3], Munjiza first introduced them into the 3D FDEM code. The contact detection algorithm used here is called *No Binary Search* (NBS) contact detection algorithm [3]. This algorithm is very computational efficient because both the RAM space M and the CPU time T required for detection only increase linearly with the increase of element number *N* (**Eqs. (8)** and **(9)**).

$$M \propto N \tag{8}$$

$$T \propto N \tag{9}$$

The contact interaction algorithm used to handle the mechanical contact is based on the penalty function method [3, 12]. In this algorithm, penetration between discrete elements will generate a pair of contact forces, which are equal and opposite acting on the two elements of a contacting couple.

The contact force $\boldsymbol{f}_{contact}$ generated due to penetration is then calculated as:

$$f_{contact} = \sum_{i=1}^{m}\sum_{j=1}^{n}\int_{V_{ij}=\beta_{c_i}\cap\beta_{t_j}}\left(grad\ \varphi_{c_i} - grad\varphi_{t_j}\right)dV_{ij} \tag{10}$$

where dV_{ij} is an infinitesimal overlap between contactor element β_{c_i} and target element β_{t_j}, m and n are the total number of tetrahedral elements into which the contactor and target discrete elements are discretised, φ_{c_i} and φ_{t_j} are potential functions for the contactor element β_{c_i} and target element β_{t_j}, respectively.

Sliding friction is also considered as a type of contact. A Coulomb friction law exists in the three-dimensional FDEM code, which is in the form of:

$$f_r = \mu N \tag{11}$$

where f_r is the friction force, μ is the friction coefficient, N is the pressure acting in the normal direction of the contact plane. Therefore, sliding along the tangential direction will occur when:

$$f_{tan} \geq \mu N \tag{12}$$

where f_{tan} is the contact force in the tangential direction of the contact plane.

2.5 Fracture Model and Mohr-Coulomb Criterion in FDEM

The fracture model in FDEM establishes the connection between the finite element formulation and the discrete element formulation. Prior to fracture initiation, the stresses in each intact discrete body are calculated using the finite element formulation. If the stress state satisfies the failure criterion, a discrete fracture is formed, and the interaction between the discrete fracture surfaces is explicitly modelled using contact algorithms in the discrete element

formulation. This allows for capturing the realistic and accurate transition from continuum to discontinuum behaviour.

The stress-displacement relationship in **Figure 2** is defined by three key parameters: peak stress (f) representing material strength, maximum elastic displacement (δ_p), and critical displacement (δ_c). G_f represents the fracture energy, which is defined as the area under the stress-displacement curve after failure. For the normal stress component (σ_n), it corresponds to the tensile strength (f_t), while for the shear stress component (τ), it represents the shear strength (f_s). In this model, the tensile strength (f_t) is assumed to be constant, whereas the shear strength (f_s) is determined by the Mohr-Coulomb criterion with a tension cut-off.

$$f_s = \begin{cases} c - \sigma_n \tan\phi, & if\ \sigma_n < f_t \\ c - f_t \tan\phi, & if\ \sigma_n \geq f_t \end{cases} \quad (13)$$

Here, cohesion (c), internal friction angle (ϕ), and normal stress (σ_n) acting perpendicular to the shear direction are taken into account. It is important to note that the engineering mechanics sign convention is used, where tensile stress is positive and compressive stress is negative.

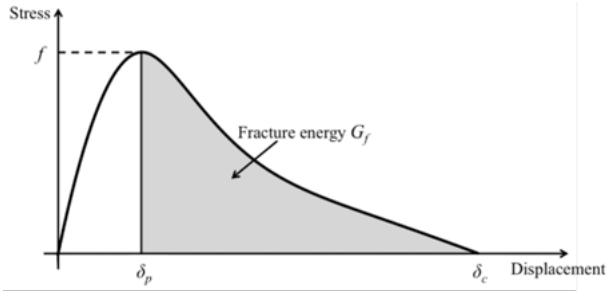

Figure 2: Stress-displacement relationship for joint elements

The solid rock mechanical (FDEM) model can then simulate the rock destruction process of the jet's hydraulic loading. For a microstructure-based model representation of the rock properties, the FDEM solver simulates the destruction process by modelling the cracking within minerals and along mineral boundaries, the crack coalescence and fragment formation and finally, fragment and chipping interactions and movement away from the intact rock to leave behind a crater or groove. The fragment removal is reliably predicted to be the result of the jetting, provided the FDEM model has instructed the appropriate jet-induced forces to be applied at the boundary of the rock domain in the correct way, see **Section 2.6** below. Also, if the model is for jetting in deep geothermal drilling conditions, representative bottom hole back pressures and geostatic stress states need to be applied correctly at the rock domain boundaries. Note that a continuum FEM solid model will not explicitly resolve the mechanics (i.e. motion and contact) of breaking pieces and their removal as fragments and chippings, whereas FDEM is ideal for these cases.

2.6 Representation of HPWJ Erosion Forces as Pressure History Boundary Condition in FDEM Domain

2.6.1 Recap of CFD Simulations in D5.1

It is important to recall that in D5.1, a CFD model was described that computed a specific exit velocity profile from the jet according to the applied jet chamber pressure. Several such profiles

are shown in **Figure 3**, from which the flow inside the pressure cell rig was computed with an adaptive meshing CFD code (IC-FERST) and the impinging pressure profiles were derived as shown in **Figure 4**. A quadratic best-fit function is used to generate the axisymmetric spatial distribution function of the impinging pressure to be used in the model.

The arrival of the jet on the surface happens very fast – within 0.1 of a msec and creates a strong water-hammer effect. It is possible to ramp the spatial pressure distribution over such a time, to reach the maximum impinging pressure distribution.

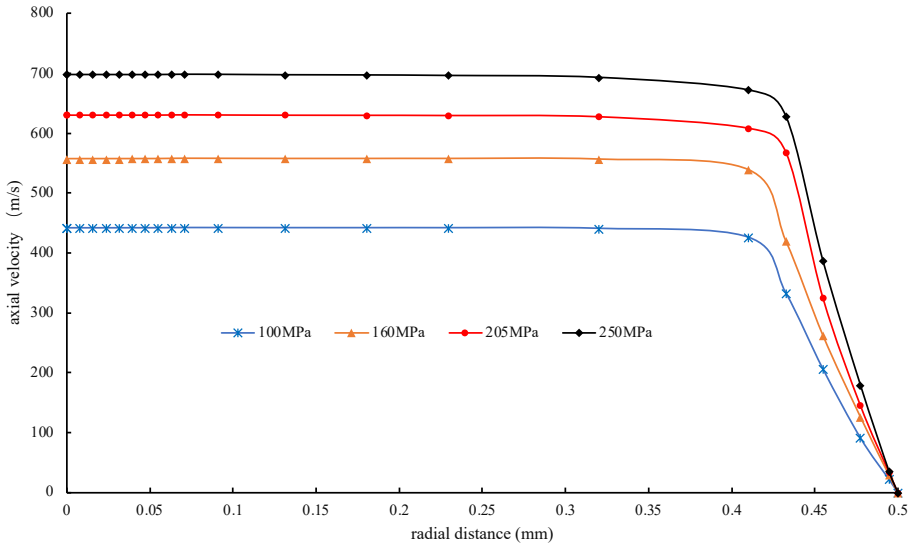

Figure 3: Orifice exiting velocity profile along radial direction as derived from CFD models of UPC, (see ORCHYD Internal Report Deliverable D5.1 “Report on Jetting with Different Mud Fluid Properties”, September 2021).

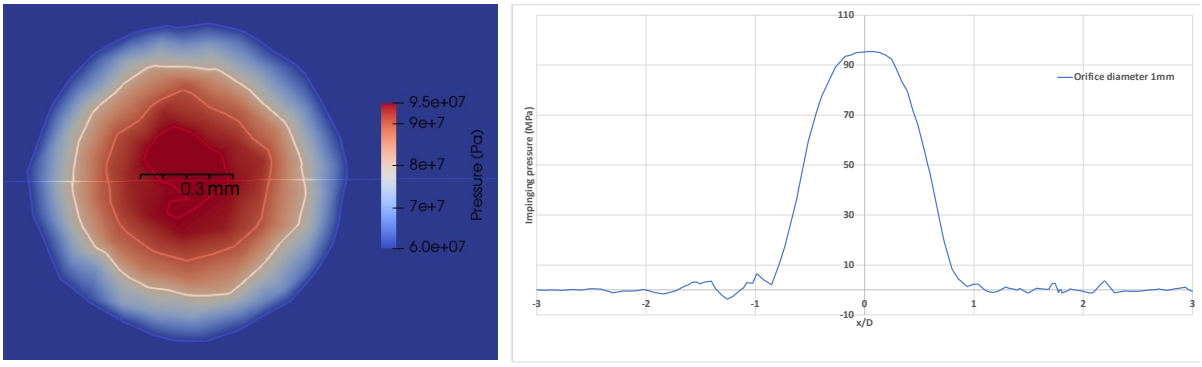

(a) **(b)**

Figure 4: For standoff distance = 3 mm, nozzle diameter = 1 mm, nozzle chamber pressure = 100 MPa: (a) pressure contours of the impinging bottom surface of jet; (b) pressure distribution along x direction on the bottom surface (see ORCHYD Internal Report Deliverable D5.1 “Report on Jetting with Different Mud Fluid Properties”, September 2021).

2.6.2 Pressure History Boundary Condition Model for Progressive Rock Penetration

A fully two-way fluid-solid coupled numerical model has been applied by the ICL team in previous EU SURE projects [1]. This model is capable of modelling the most critical processes

in HPWJ: 1. the impact of high-speed jet; 2. initiation and propagation of cracks; 3. fragment removal. Due to the expensive CPU cost, this model is limited to a small-size simulation domain with short simulation time. Therefore, to simulate HPWJ within more reasonable run-times, a new one-way fluid-solid coupling model is developed and used in this research for ORCHYD, i.e., the fluid model (CFD) is separated from the solid model and fluid velocity and pressure fields are treated as boundary conditions to the solid model.

To simulate the high pressure water jet and rock interaction, temporally varying boundary conditions are also applied to account for the evolving rock geometry of the evolving crater. Adopting several simplifying assumptions, it is possible to determine isolated fragments to be removed from the solid model. It is important to include the effect of increasing distance of the rock surfaces from the nozzle, should the jet erode the rock. The spatial impinging pressure is updated if pressure reduces due to sufficient deepening of the rock surface, possibly due to the weakening power of the core of the jet which begins when the standoff distance is 7 to 10 times the nozzle diameter, a threshold proved in D5.1. A more important effect in the model scenarios to be taken into account is the creation of new surfaces at varying angles. Normal stress perpendicular to all sloping new fracture and crater wall surfaces is therefore applied, hence the term pressure history boundary condition. The jet-rock interaction is therefore a one-way coupling approximation applied using a novel approach.

2.7 New Features Implemented in FDEM: Defect Intensity

Granite, an igneous rock known for its durability and strength, is not exempt from the presence of structural features, including defects such as microcracks (e.g. **Figure 5a**). These microcracks are minuscule fractures or fissures within the rock, often so tiny that they remain imperceptible to the naked eye and may even elude detection under a microscope.

For shallow sub-surface rock engineering and in construction with rock-like geomaterials, crack propagation is commonly associated with tensile stress and tensile failure and the role of defects and micro-cracks acting as flaws and stress risers is well understood in fracture mechanics theory. For the deeper sub-surface, high in-situ bottom hole fluid pressures and confining stresses that will be experienced at drilling depths of say 4 to 5 km, the understanding of the role of microcracks is less clear.

Microcracks/defects can be incorporated into FDEM numerical models by introducing pre-existing broken joint elements within the mesh structure, as illustrated in **Figure 5b**. In the scenarios described below, the material properties for the ‘broken’ joint elements (including cohesion, tensile strength, and energy release rates for modes I and II) are typically adjusted by reducing their normal values by a factor of 1000.

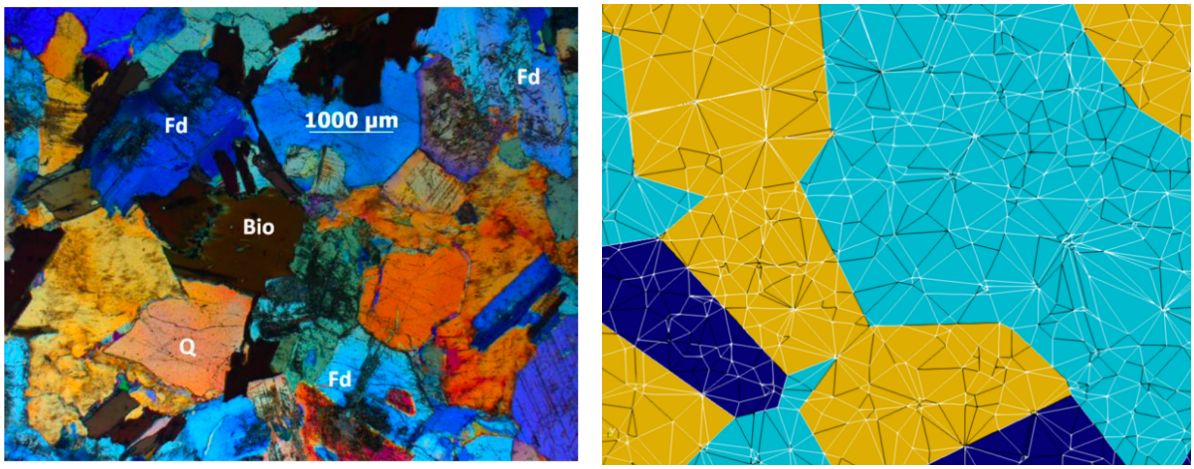

(a) (b)

Figure 5: (a) Observations under cross-polarized light of the Sidobre (Silverstar) granite. (b) Shown here is a cross-sectional view of a 3D FDEM numerical model, where minerals are represented in different colours. The white line segments denote the joint elements, while the black segments signify pre-existing broken joint elements.

2.8 Microstructure-Based FDEM Model

2.8.1 Introduction and Challenges

A rock fragmentation numerical model of the jet pressure's effect on the rock destruction process, capable of investigating the range of conditions to be applied in the confining pressure cell in the ARMINES Labs, was developed with the methodology described above. Research on the microstructural modelling in Task 5.4 presents several key challenges for which solution strategies have been devised, as described below.

i. ***Calibration of rock microstructure-based simulations:*** To calibrate a microstructure-based fracture model, it is necessary to identify many unknown materials input parameters for each phase (i.e., mineral) and interface among different phases – e.g., there are 42 unknown parameters for granite composed of three phases. Traditional trial-and-error methods to calibrate the micromechanical properties based on the macroscopic mechanical properties have a high risk of achieving only low accuracy. Also, they can lead to unreasonably expensive computations due to a large difference in length scales between domain and microstructural features. Therefore, a new experimental approach is required to characterise the micromechanical behaviour of rocks which effectively serves the calibration of microstructure-based models. However, data of this kind that is relevant to the ORCHYD rock suite in question is extremely limited.

ii. ***Long run times for rock microstructure-based simulations:*** In general, the non-linear stress and strain fields of microstructure-based models are inevitably expensive because of (i) large number of elements and (ii) small elements required to explicitly simulate microstructure geometry. This was known beforehand to be a limiting factor for the length of time the jetting action can be modelled. It affects the resultant traversing distance that can be modelled which depends on rotation rate and radial distance. If the RPM in the experiment is changed from an expected RPM for mud-hammer of ~40 RPM to ~4 RPM, the same traverse distance in the experiment e.g., of

20 mm, must be traversed in the numerical model's identical virtual experiment and therefore the simulation run time will be 10 times longer. A 2-day simulation becomes a 20-day simulation, which is impractical. To simulate the ~1-2 RPM test traverse as presented in the preliminary ARMINES lab tests is therefore highly problematic.

2.8.2 Strategy for Multiscale Mechanical Characterisation of Rock and Domain Scales of ORCHYD

To address the first challenge, the ICL team devised an integrated experimental program aimed at calibrating microstructure model parameters. This calibration used rock blocks obtained from the sample suite, consisting of 50 mm cubes from three different granites provided by ARMINES. Among these, the Sidobre granite was selected as the "base case" granite type due to its coarser grain size, which allowed for the use of larger elements in the numerical simulation (i.e. fewer element), resulting in faster run-times. However, it is essential to consider that when subjected to local contact loading conditions of the jet in the range of 1 mm to 4 mm, the rock's response is likely to exhibit significant variability. This variability is dependent on the microstructural heterogeneity (i.e. granular structure configurations) of the rock immediately encountering the applied loads.

Figure 6 provides an overview of the methods employed for characterising the mechanical properties of rock at multiple scales. The process begins with the calibration and validation of a new model that incorporates microstructural features specific to Sidobre granite. Initially, ICL conducted experiments to determine single-crystal (i.e., single-phase) mechanical properties. This involved integrating mineral mapping and nanoindentation tests, with collaboration from external university laboratories, specifically the University of Bristol. Subsequently, the material properties identified at the crystal level were utilised in the calibration of 10-millimeter Brazilian disks at the polycrystal level, as part of an upscaling strategy. During this stage, numerical simulation methods were combined with experimental approaches, including tensile indirect tests coupled with Digital Image Correlation (DIC) and XCT. The calibration process then extended to the jetting scale, where the objective was to characterise all mechanical input parameters relevant to this dynamic loading regime.

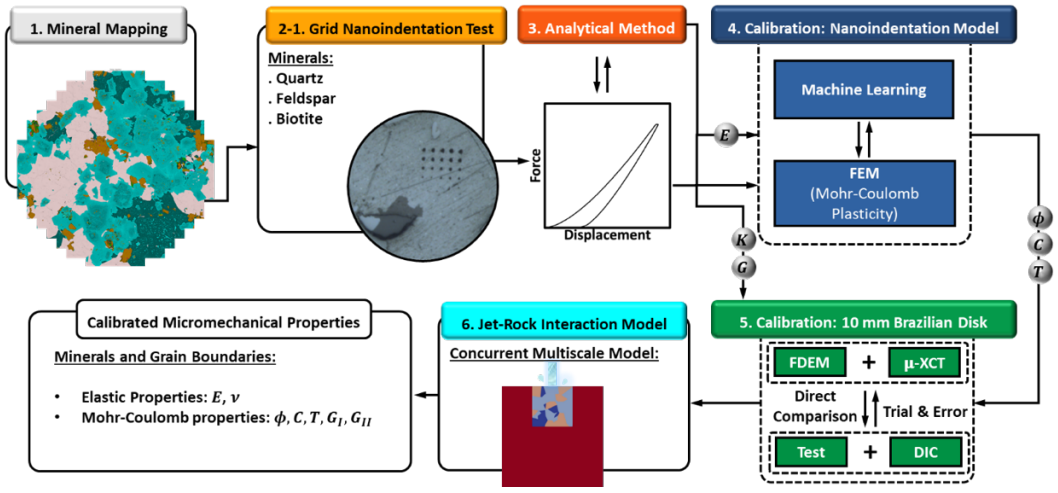

Figure 6: Framework for three-level multiscale characterisation and calibration of granite micromechanical properties using coupled experimental, numerical and machine learning methods.

The details of the methodology are included in a paper in preparation Naderi et al. AI-Assisted Multi-Level Characterisation of Crystalline Rock Mechanical Properties)

In summary, the specimen of Sidobre that was mapped with TIMA at NHM was polished and prepared for nano-indentation testing. A representative selection of Sidobre (SD) feldspar, quartz and biotite crystals were subjected to grid nano-indentation tests to provide the essential force displacement plots for each phase. A combination of theory, and several simplifying assumptions including that the crystal phases behave as Mohr-Coulomb plastic solids are then applied. Machine learning algorithms use characteristic signature values from the force displacement plots as inputs, and the best fit material property values of C, ϕ and UTS were determined as outputs for each of the three SD mineral phases to complete stage 4 of the first-level characterisation, as shown in **Figure 6**.

At the second level and upscaling to the polycrystal 10 mm size of the Brazilian disc, X-Ray CT raw data from the Sidobre 10 mm Brazilian disc specimen was successfully converted to a three mineral phase 3D model. This required advanced methods including removing beam hardening artefact, and segmentation to be applied to allow for the feldspars and quartz to be reliably distinguished. After further necessary geometric simplifications, the disc model was meshed at appropriate resolution and could be subjected to Brazilian Disc virtual testing by multiple FDEM mechanical simulations, each with different sets of intra and inter-crystalline material properties. The matching Brazilian disc indirect tensile strength tests were also performed on Sidobre rock discs in the Structures Lab at ICL. The closely monitored failure response of real rock specimens was then compared with deformation and failure of their directly equivalent microstructure-based models. The trial-and-error calibration of material parameters for FDEM modelling of the Sidobre granite in quasi-static tensile failure, by the direct comparison approach is schematically summarised in step 5 of **Figure 6**.

Figure 7a shows the FDEM disc model after failure with exaggerated crack apertures and also illustrates the location of the main felspar, quartz and biotite crystals that were present in the laboratory test specimens which were carefully aligned to have the correct loading positions for a good match. **Figure 7b** gives an indication of the sensitivity and importance of property calibration showing the effect of halving the two of the dominant parameters, G_I and T (i.e., UTS). DIC was applied during laboratory testing (**Figure 8**) as a means to further examine the similarity in style of crack formation in such small coarse-grained domains between model and experiment.

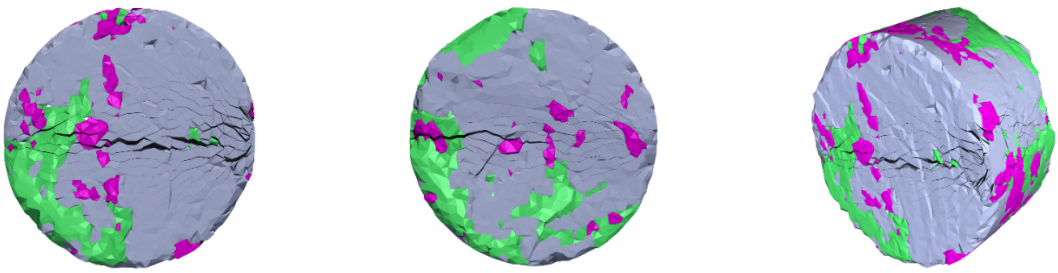

(a)

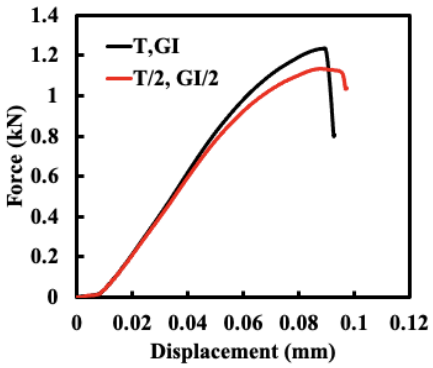

(b)

Figure 7: Microstructural model of Sidobre granite 10 mm diameter 5 mm thickness Brazilian disc test: (a) Failure mode of XCT based model with crack aperture shown ×10 for clarity from different views (green: quartz phase, grey: feldspar phase, pink: biotite phase); (b) force displacement curve for different tensile strength and energy release parameter settings of all three phases.

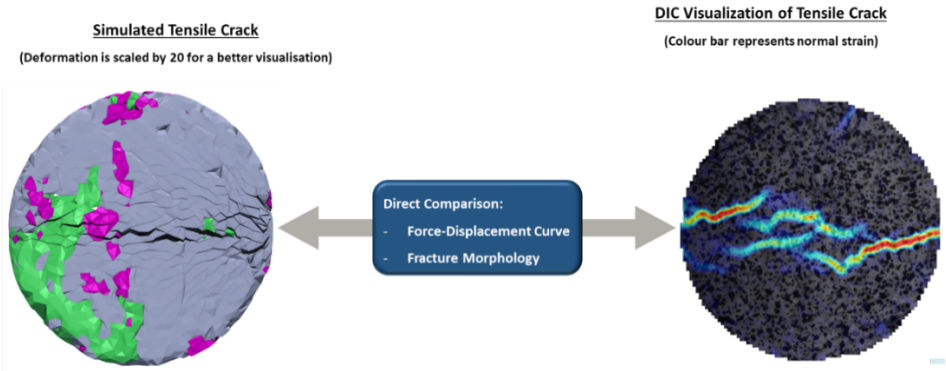

Figure 8: Brazilian disc failure comparing tensile crack morphology of FDEM simulated crack apertures (exaggerated) and DIC captured visualisation of localised strain of failing experimentally loaded disc specimen

In the final stage, as depicted in **Figure 6**, the characterised mechanical parameters can later be employed in Voronoi-based microstructure models for various loading scenarios. These scenarios may encompass both jet-rock models in WP5 and insert-rock models in WP6. Details of the calibration method under jetting conditions are presented in the subsequent section.

It is important to point out that the absence in the original work task schedule for generation of the needed X-Ray CT data stimulated this ambitious new initiative to accelerate the data acquisition and the strength testing of small Brazilian disc specimens. Unsurprisingly, strength testing of coarse-grained 10 mm diameter discs introduced practical problems requiring specially built features to adapt rigs in the laboratory and the good-will and time from experts in ICL's Structures Lab. This additional experimental work drawing on extremely generous help from the Natural History Museum, Bristol University, ICL's Labs (Rock Preparation Lab, X-Ray CT Lab, Structures Lab), eventually generated a coherent body of data.

3 Study

It is very important to validate the numerical model before it is applied to simulate the HPWJ. In this research, the validation process has two levels:

1. The microstructure model is constructed, calibrated, and validated by 10 mm Brazilian compression tests. The detailed procedure has been described in Section 2.8.
2. The numerical model for HPWJ is further validated by jetting experimental tests under confinement. In this procedure, the Defect Intensity percentage parameter (DI) is calibrated. This procedure is described in the following section.

3.1 Calibration and Validation Process

The validation study consists of several stages.

i. The benchmark case for jetting condition variables needs to be determined. Experimental and numerical model jetting duration time must be equivalent and for this it was agreed that ~0.2 s *non-traversing* jetting would be applied. The accuracy and precision (reliability) of the experimental result(s) for benchmarking is an important consideration. Then the most meaningful magnitudes of all the controllable jetting variables (back pressure, jet pressure etc.) are set as the benchmark conditions.

ii. Experiments are performed with this set of base-line conditions forming the benchmarking case for the very specialised dynamic localised jetting application of the model.

iii. The numerical microstructure model is constructed using a Voronoi-based approach to generate representative microstructures of Sidobre granite within a small cubic volume of rock, situated within a larger cubic domain of homogeneous rock. The larger surrounding cube is assigned average engineering macroscopic density and elastic properties, representing an undamaged state – these properties are determined based on the new strength testing experiments, which have been uploaded to the ORCHYD project database. The model described here constitutes a concurrent multiscale microstructure, as schematically illustrated in **Figure 9**.

iv. Numerical models of the jetting process are run for the benchmark case, first with the calibrated parameters that were validated for the 10 mm Brazilian disc compression tests.

v. A systematic study of the effect of DI in the range of 5-95% was performed. It is observed that the larger the DI, the deeper are the grooves generated. A value of 30% was selected for the DI parameter as it provides a good match when compared with the experiment – under benchmark conditions for the validation criterion used. Here we use maximum depth of groove. Other criteria such as volume of removed rock are also possible. In future work it is hoped that the sensitivity of the DI parameter can be further investigated with respect to volume of removed rock.

vi. These settings are applied to model grooving for a suitable *traversing* jet test.

vii. 'Blind Test' prediction may be possible for a parametric study of various traversing jet conditions.

The principal destructive mode of interest is in fact a traversing jet. The traversing speed to be tested experimentally needs to be in the range of interest for practical bit operation, a function of rotating bit RPM and radial distance from the nozzle orifice to the axis. It is then of great

interest to evaluate whether the model calibration parameters validated for the non-traversing case can be used to predict grooving depths of the traversing jet experiments. For these, the jet is moving some 5 mm/s or more at 157 mm/s which is in the velocity range for the jet power per unit area to fall within a range of interest for practical peripheral grooving while drilling. If model results prove to be of satisfactory quality in predicting the main difference or trend between depths for non-traversing and traversing cases, that will provide the reassurance to move beyond the validation study to a new level. This can be referred to as 'Blind Test' prediction, for which there may or may not be any experimental data.

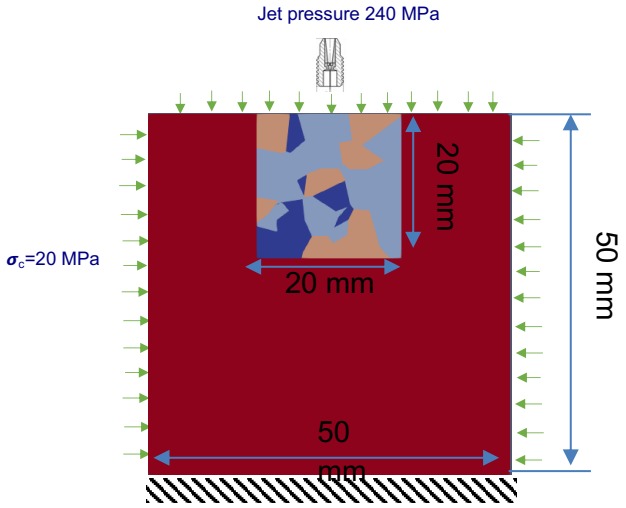

Figure 9: Schematic of concurrent multiscale model, representing non-traversing jetting and its configuration as described in Stage (iv) of the validation study.

3.2 Calibrated Material Parameters

The microstructure-based model of Sidobre Granite (SD) was calibrated using the two-level approach as described in **Section 2.8.2** and illustrated in **Figure 6**. The calibrated parameters are given in **Table 1**. The calibrated continuum properties of the pure mineral phases ρ, E, ν are assigned to the finite element tetrahedra. All other properties: friction coefficient $Tan(\phi)$, cohesion C, unconfined tensile strength T, Modes I and II critical energy release rates G_{IC}, G_{IIC}, are the fracturing-related strength variables for which calibrated parameters are assigned to the joint elements. There are several alternative roles played by the joint elements which act to represent potential fracture paths. These paths can be either within crystals (intra-grain) or along boundaries between crystals (inter-grain). Furthermore, the joint elements can be specifically activated as part of the Defect Intensity algorithm such that they acquire the properties of a flaw (i.e., defect or microcrack). This is illustrated with reference to Table 1 by considering the case of all joint elements concerned with the mineral phase Quartz:

(i) within a pure crystal phase with no flaw e.g. see row for Quartz,

(ii) where the *DI* parameter has randomly assigned a joint element to lie within a certain crystal phase and represents weakening by a flaw, e.g., see row for Quartz (Microcrack),

(iii) where there is an inter-crystal phase boundary with no flaw, e.g., see row for Quartz-Feldspar,

(iv) where the *DI* parameter has randomly assigned a joint element to lie within an inter-crystal phase boundary and represents weakening by a flaw, e.g., see row for Quartz-Feldspar (Microcrack),

(v) where there is an inter-crystal phase boundary with no flaw, e.g., see row for Quartz-Biotite,

(vi) where the *DI* parameter has randomly assigned a joint element to lie within an inter-crystal phase boundary and represents weakening by a flaw, e.g., see row for Quartz-Biotite (Microcrack).

Note that as the model domain employs a concurrent multiscale model with a limited volume for the crystal representation of interest embedded in a surrounding medium of a macroscopic average properties, the table includes a row of properties labelled 'Macro'.

Table 1. Material properties of the microstructure-based model of Sidobre Granite (SD).

Mineral/Interface	ρ (kg/m^3)	E (GPa)	ν	Tan(ϕ)	C (MPa)	T (MPa)	G_{IC} (N/m)	G_{IIC} (N/m)
Quartz	2650	48.19	0.17	1.746	126.98	18.70	11.60	34.80
Quartz (Microcrack)	2650	48.19	0.17	1.746	1.2698	0.1870	0.116	0.348
Feldspar	2560	45.55	0.2	1.1066	94.45	16.88	5.80	17.50
Feldspar (Microcrack)	2560	45.55	0.2	1.1066	0.9445	0.1688	0.058	0.175
Biotite	3050	23.62	0.29	0.85769	50.30	17.56	2.10	6.30
Biotite (Microcrack)	3050	23.62	0.29	0.85769	0.5030	0.1756	0.021	0.063
Quartz-Feldspar	-	-	-	0.343	77.50	6.225	3.05	18.30
Quartz-Feldspar (Microcrack)	-	-	-	0.343	0.7750	0.1245	0.0305	0.183
Quartz-Biotite	-	-	-	0.318	62.05	12.69	2.4	14.40
Quartz-Biotite (Microcrack)	-	-	-	0.318	0.6205	0.1269	0.024	0.144
Feldspar-Biotite	-	-	-	0.277	50.66	6.025	2.40	8.30
Feldspar-Biotite (Microcrack)	-	-	-	0.277	0.5066	0.06025	0.024	0.083
Macro	2630	67.3	0.27	1.08	22.9	8.9	0.1	1

3.3 Experimental Data from Non-Traversing Jetting Tests

The jetting experiments used to calibrate and validate the microstructure-based jetting model for Sidobre Granite (SD) were conducted in the pressure cell at Pau and were designed in consultation between ICL and ARMINES for the purpose of calibrating the numerical model, as described in D5.3. To remove experimental uncertainties, the simplest reproducible setup (excluding the inevitable rock heterogeneity effects) and jet condition combined with the shortest simulation time would be a short duration non-traversing jetting test. This would minimise the apparent uncertainties associated with the experimental rotation rate for short tests since it would be almost impossible to set the jet traversing rate to be applied to the model to be a good match with the rates in the experiments.

The time over which the jet is actively jetting on the same spot could not be controlled to a high level of accuracy for such short durations but could be back calculated. Knowing the results of such a coarse crystalline rock tend to vary widely from place to place it was essential also to try non-traversing jet grooving on several separate specimens (5 in all) of the rock and with four separate locations for each specimen to sample the variability. For the benchmark conditions of this test, Back Pressure 20 MPa, Chamber Pressure 240 MPa, Standoff Distance 4 mm and jet nozzle diameter 1.0 mm were applied. The scatter in maximum crater depth for a range of short durations are given in **Figure 10**.

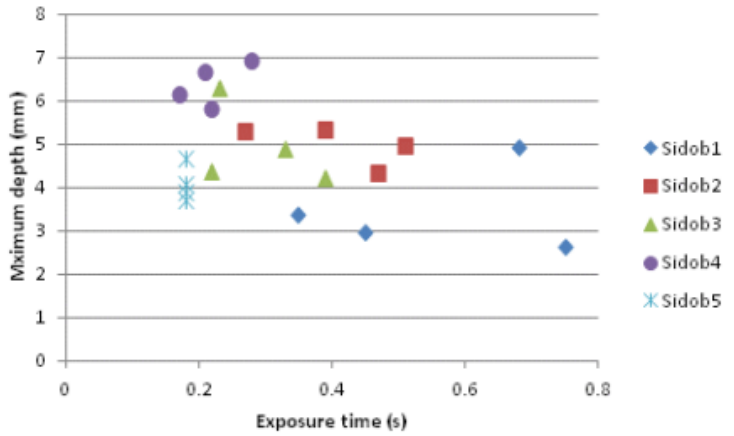

Figure 10: Non-traversing jetting tests on Sidobre Granite (SD). For jetting conditions, see text.

3.4 Experimental Data from Traversing Tests

Results of the tests described in D5.3 for traversing tests (new plate) are presented in **Figure 11**.

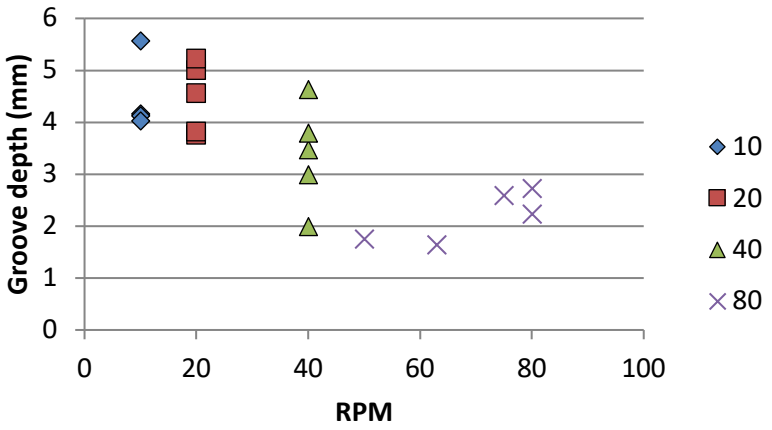

Figure 11: Results of Depth of Groove for Benchmark testing conditions on SD rock at varying rotation rates. Note at 20 RPM, traversing velocity is 0.157 m/s and for this condition, brown symbols correspond to the benchmark condition i.e., 20 MPa back pressure.

The methods used and results obtained were explained in D5.3. At 20 RPM the jet traverses the 10 mm open slots of exposed rock surface (the remainder is covered in steel plate) in just 0.063 s although making a depth of groove comparable to the stationary jet acting for a duration of 0.2 s, some 3 times longer. Traversing the jet is therefore more efficient in creating depth than a stationary jet, however when the jet traverses at faster rates, the groove depth reduces. The greatest depth is suggested by the experimental results in **Figure 13** to be somewhere between 0 and 10 RPM.

3.5 Microstructure-based Model of Sidobre Granite – Non-traversing

3.5.1 Model Configuration

Figure 9 shows a schematic of the concurrent model composed of the Voronoi-based microstructure of SD, which is embedded in a homogeneous domain. The green arrows

symbolise the hydrostatic confining pressure boundary conditions such that bottom hole back pressures are 20 MPa as well as the horizontal and vertical confining pressure in the rock. The base of the rock cube is fixed to have zero displacement in all directions. Gravity is active. The pressure boundary condition applicable to inlet velocities with the top hat profile for the 1 mm diameter orifice nozzle, driven by a chamber pressure of 240 MPa is applied locally to the centre of the surface of the microstructure model domain. These conditions match those used in the pressure cell rig for the benchmark case. The example is provided for validation purposes, where back pressures of 20 MPa for a 2 km deep hole are reasonable, although the geostatic confining stresses would need to be about 2.5 times higher to be realistic for 2 km depth.

3.5.2 Sensitivity analysis of Defect Intensity for Non-traversing Jetting

The DI parameter and the significance of having pre-broken joint elements, was introduced in **Section 2.7**. To illustrate the sensitivity of this parameter and how DI was calibrated for the non-traversing jetting case, see **Figure 12**. As DI as a percentage is increased from 20% to 25%, the jet action generates cracking to a greater depth but no further volume or depth of removed fragments is suggested along this line of section through the jet axis and crater. However, once DI is set at 30%, there are sufficient increase in numbers of joint elements with greatly reduced strength properties to promote cracking and fragments shown as being removable. *In this context a fragment is mineral material isolated by being surrounded by broken elements*. The algorithm to remove the fragments, leaving behind grey space, does not distinguish broken rock that is not connected to the free surface from that which, hence the deep ‘holes’ shown. In more recent work, a sophisticated algorithm is used to remove only those fragments that are not locked down to the main intact rock.

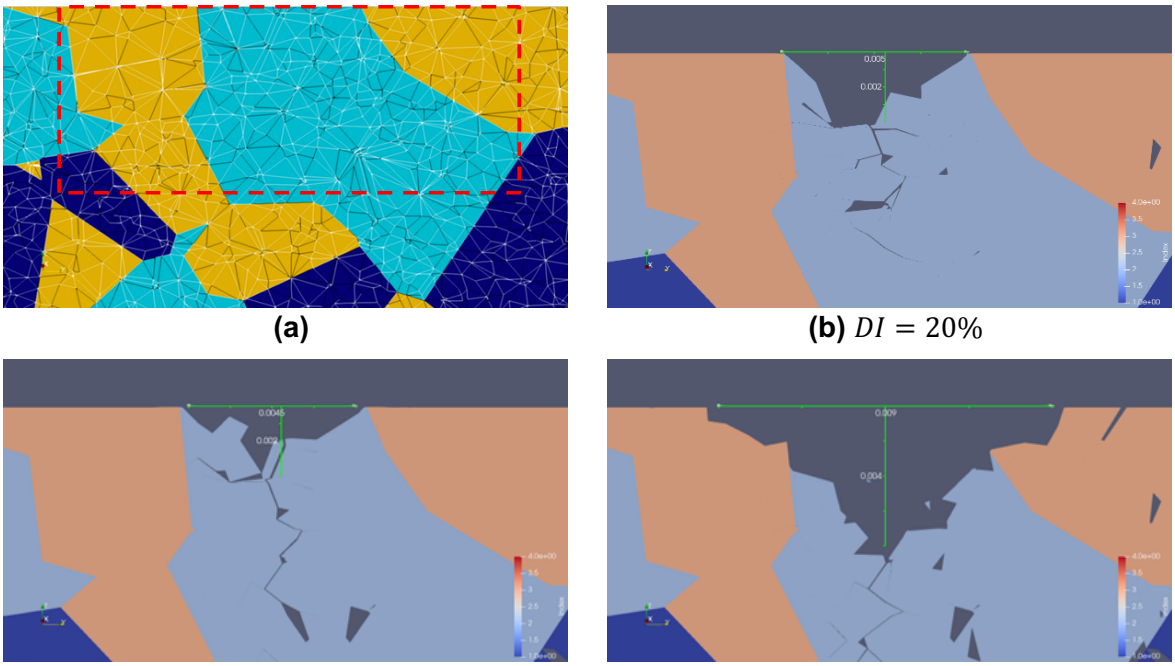

(a) **(b)** $DI = 20\%$ **(c)** $DI = 25\%$ **(d)** $DI = 30\%$

Figure 12: Calibration of Jetting Depth with Defect Intensity. (a) Displays 30% of all defects highlighted with black lines. (b), (c), and (d) illustrate models with Defect Intensity (DI) set at 20%, 25%, and 30%, respectively. The FDEM simulation results in the formation of discrete fragments and cracks (i.e., groove structures), which are visible as empty spaces against a grey background.

3.5.3 Effect of Heterogeneity and Crystal Sizes with Respect to Jet Diameter

For non-traversing conditions it will make a big difference what crystals lie in the target zone because at the jet scale the rock is highly heterogeneous. **Figure 13** shows the set-up and **Figure 14** illustrates the corresponding simulation results for different locations of the jet. The benchmark conditions modelled are: Confining pressure 20 MPa, Back pressure 20 MPa, Chamber pressure 240 MPa, Stand-off distance 3 mm, Nozzle diameter 1 mm, and the Defect Intensity is 30%.

Clearly, the jetting hole depth can be seen to vary considerably, the range captured here being between 6 mm (biotite boundary) and 2 mm (quartz) and this spread is compatible with the randomly repeated non-traversing jetting results shown in Figure 12. The numerical model appears to suggest that axial (or median) cracks tend to preferentially develop. One explanation for this is that the cracking is occurring as a result of the equivalent process to the “water hammer effect” as postulated for the relative effectiveness of pulsating water jets as compared with continuous jets.

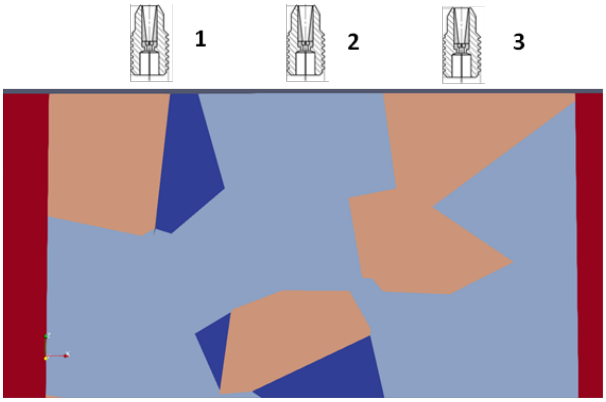

Figure 13: Cross-Sectional view of three jet impact locations for assessing 3D microstructure-based model predictions of jet location effects, emphasizing result variability due to the inherent heterogeneity of the SD rock at this loading scale. Samples were taken from different positions of jet impact: 1. Biotite/Quartz grain boundary area, 2. Feldspar, 3. Quartz, illustrating depth variability in the tests for a more comprehensive understanding.

(a) Location 1

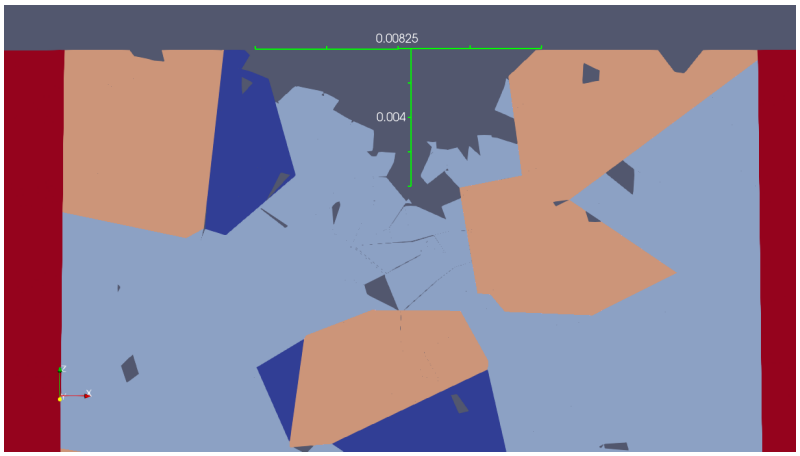

(b) Location 2

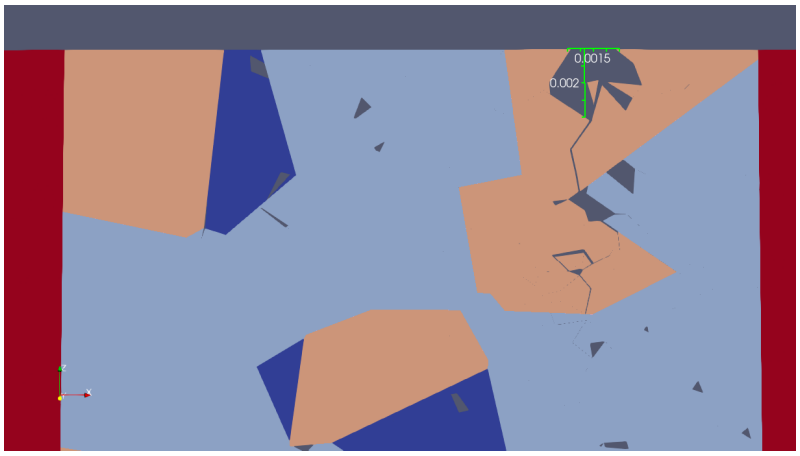

(c) Location 3

Figure 14: The simulation of grooves corresponding to the locations described in **Figure 13**.

3.6 Microstructure based model of Sidobre Granite – Traversing Jet

In the previous section, the model is arranged with the jet striking the middle of a feldspar grain and this is perhaps a good starting point for the calibration case as this phase is well over half of the rock's constituents. In considering the effect of a traversing jet, the model boundary conditions are set up to have the appropriate jet pressure distribution displaced at a steady

velocity of 157 mm/s as this corresponds to the bit rotation speed of 20 RPM and a jet located 75 mm from the centre, the nozzle distance set up in the pressure cell jetting tests.

3.6.1 Simulation of Starting Point Effect

In the first traversing simulations, we investigate the difference made by the starting point selected for the simulation. The boundary conditions are schematically shown in **Figure 15**.

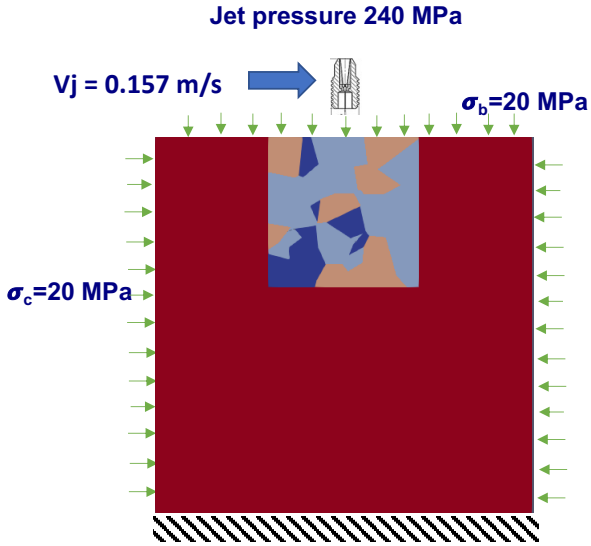

Figure 15: Boundary conditions for the traversing jet model. Jetting is started at two alternative locations, the centre of the feldspar crystal or at the point above the biotite/feldspar crystal boundary.

The consistency between the two distinct results at groove depths of 4.5 mm and 6 mm, as depicted in **Figure 16**, is highly reassuring. This alignment with the experimental data, which shows a range from 3.8 mm to 5.2 mm, suggests that starting point effects and inherent heterogeneity provide plausible explanations for the observed variability in the experimental data shown in **Figure 11**.

It is largely a coincidence that the jetting depth is of a similar magnitude or only slightly greater than for the non-traversing cases simulated since about 3 times less jet energy has been applied in the case of the traversing jet over its 10 mm path. It is interesting to speculate on the reasons why the traversing jet would be more effective. Dehkhoda and Hood (2013) investigated pulsed jets and described the water hammer effect in jet rock interaction in submerged conditions. It has been suggested [1, 13] that a modelled water-hammer effect was responsible for the rock destruction in a fluid-solid coupled simulation of jetting in submerged porous sandstone. In the work reported here, the simulation applies a pressure boundary condition that varies in time and space to an impermeable rock. It seems reasonable to suggest that the effect of the jet core's relatively sudden arrival on new rock surface (and change in local state of stress) is captured although the impact of the pressure history profile and its relationship with the water hammer effect is a subject worth exploring further. It is to be expected (in terms of jet energy arriving per unit length traversed) that the model would show an increase in average depth of groove for 10 RPM (79 mm/s for the small 75 mm jet orifice radial distance used in the pressure cell jet tests) compared to 20 RPM (157 mm/s) as seen in experiments (**Figure 11**), but that a maximum depth would occur somewhere between 0 mm/s and this velocity. However, it is important to remember that in the context of hybrid HPWJ and rotating percussive drilling, the RPM requirement of a viable drilling system is likely to be greater than 20 RPM for effective hammer action.

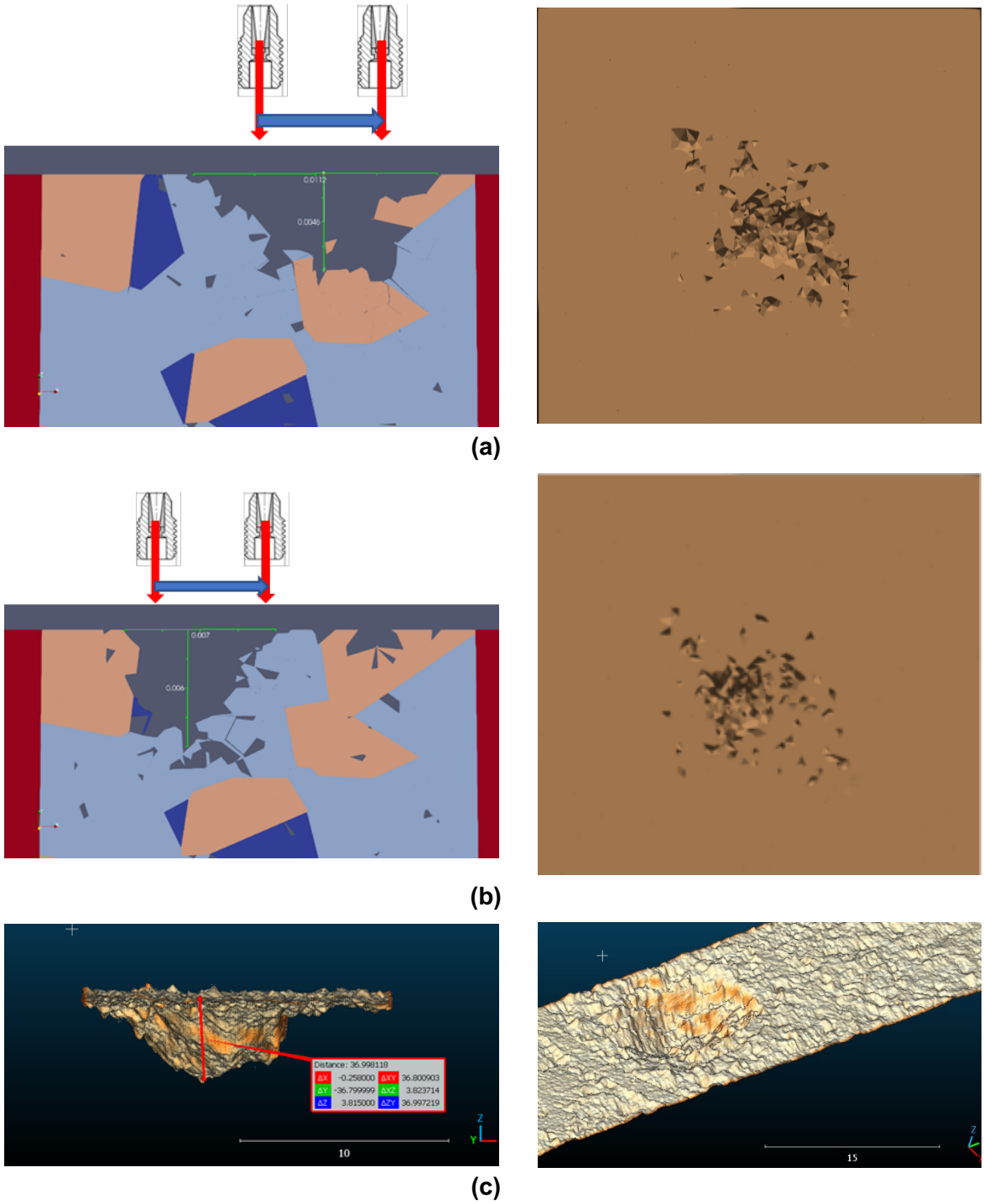

Figure 16: Traversing Jet Model and Experimental Results. Jet traverse over a distance of approximately 5 mm at a velocity of 157 mm/s, tested with two different starting points. Cross-sectional views (left column) and top views (right column) depict the simulated grooves, both within the center of feldspar (a) and aligned with the biotite/quartz boundary (b). (c) Two laser-scan visualisations of one corresponding short traversing jetting experiment (reported as TT2_4 in the data shared by ARMINES, pers comm), with crater length depth and shape of similar form but with a smother less jagged jetted surface than in the simulated grooves.

3.7 Model Prediction of Different Jetting Conditions

3.7.1 Effect of Confining Pressure, Non-traversing Jet

In this series of test simulations for the non-traversing jet we predict the difference made by changing the confining pressure applied to be different from those in the benchmark case. The boundary conditions are shown schematically in **Figure 17**.

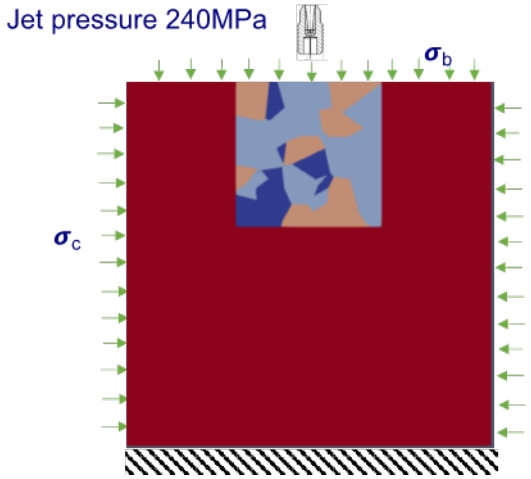

Figure 17: Boundary conditions for the non-traversing jet model. Back pressure is set equal to confining pressure, $\sigma_b = \sigma_c$ (i.e., hydrostatic state) with σ_c of 15 MPa, 20 MPa and 25 MPa.

In **Figure 18**, the meshed elements show the stress magnitude using the Von Mises stress measure with the hotter colours indicative of regions experiencing higher levels of shear stress. For σ_c =15 MPa, the depth superficially appears not very deep but there are many highly stressed elements down to depths of ~7 mm. The crater width is 6.5 mm, and a moderate volume crater was produced. For σ_c = 20 MPa, the depth is just over 4 mm with somewhat less deeply penetrating damage than for 15 MPa. However, the crater width is 9.0 mm, and a larger fragment volume has been freed by the jet. For σ_c = 25 MPa, the higher shear stress magnitudes and cracking is still penetrating to about 5 mm, however the crater volume is much less than for the other two cases as fewer flaws and fresh cracks are creating fragments at the free surface of the crater. Although these short duration jetting simulations cannot be compared directly to the 20 s jetting experiments shown in Figure 8 of ORCHYD_Deliverable D5.3, the simulations show the same trend and the depths fall within the range of experimental results that can be accounted for by heterogeneity.

Further investigation into the role of anisotropic in-situ stress fields generally is required for each drillhole depth and back pressure constraint. In particular, at 50 MPa back pressure in 5 km deep holes, horizontal stresses of ~125 MPa are to be considered. The far field in-situ vertical stress that is strongly channelled in the bottom hole environment and has been assumed to have a negligible influence in these simulations needs further consideration. However, a less expensive, e.g., mesoscale model is considered likely to be more appropriate to investigate such effects of the groove position in relation to the hole's bottom and walls and the non-uniform in-situ stress near the periphery.

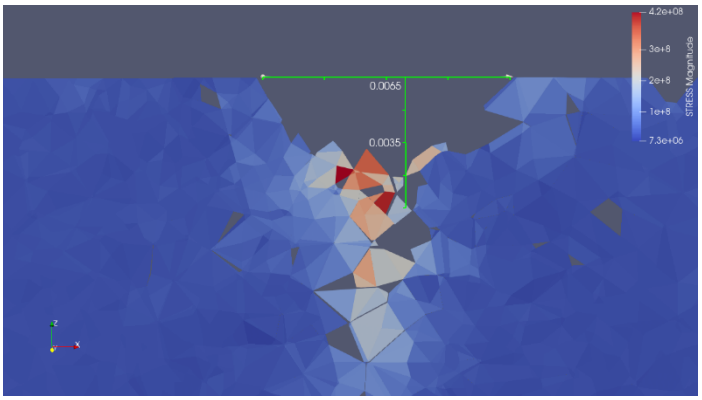

(a) $\sigma_c = 15\ MPa$

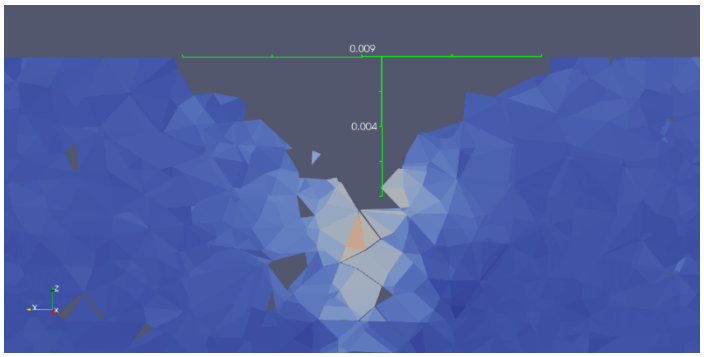

(b) $\sigma_c = 20\ MPa$

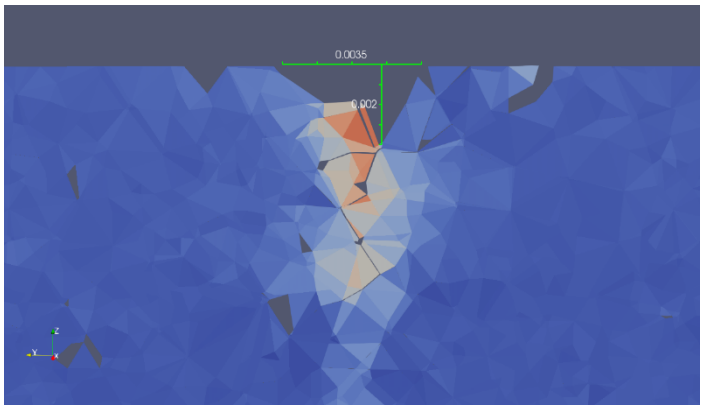

(c) $\sigma_c = 25\ MPa$

Figure 18: Microstructure-based jetting model with same region of SD granite and feldspar immediately below the jet impinging point in each case, showing effect of confining stress of 15, 20 and 25 MPa.

4 Conclusions

The microstructure of the Sidobre granite was characterised using a range of advanced experimental techniques. The micro-mechanical grain boundary and intra-grain properties, either measured or deduced, were assigned to the appropriately meshed FDEM model. A novel calibration process involving direct modelling of the load to failure of a 10 mm Brazilian disc laboratory experiment was introduced, together with nano-indentation testing and machine learning to calibrate parameter values.

Modifications to the Solidity FDEM code to simulate jetting action with a pressure boundary condition approach were made to maintain realistic pressure conditions as new fracture

surface was generated in the crater walls. The pressure boundary can vary in space and time to allow the jet to traverse and erode rock.

Benchmark experiments included non-traversing jetting tests were designed in collaboration with ARMINES and performed in Pau in the pressure cell.

To simulate the jet's groove development and rock destruction for the Sidobre (SD) granite, using calibrated model micro-parameters that exploit the Brazilian disc tests, it was necessary to introduce a further material characteristic for this granite. The introduction of an adjustable Defect Intensity (DI) parameter, a catch-all term for flaws such as microcracks and defects, was investigated during the validation study using the benchmark experimental data set. For this rock, DI was set to a value of 30% to give a close agreement between simulation and experiment for the benchmark conditions.

The heterogeneity of the granite rock, which by definition is a coarse-grained crystalline igneous rock, when viewed from the scale of the 1 mm diameter impinging pressure zone of the HPWJ, is key to understanding the range of jet responses. It is why groove or crater depth varies so much between experimental tests on the same rock block. Sidobre granite is an especially coarse granite with feldspar crystals ranging from 2 to 10 mm. Depending on the jet starting point and therefore the crystalline topology and phases immediately beneath the jet, larger or smaller volumes of mineral are broken out.

The validated non-traversing model was applied to the case of a traversing nozzle moving at 157 mm/s and for a very small number of simulations and experiments the predicted depth of the groove was remarkably similar in range and mean values to those found in the experiments.

As the traversing jet is always striking new rock, we speculate that there is a water-hammer effect of the first massive increase in locally applied pressure when the rotating bit and jet first arrives over the rock surface that is otherwise mostly experiencing only the bottom hole back pressure. If the traversing speed is too fast, there is not enough energy to create the large change in pressure in a short time. If too slow, the regime is more like non-traversing where the pressure is very high but not changing with time after the initial arrival. There is likely to be a traversing speed that maximises groove depth. This is because 10 RPM generated grooves were deeper than 20 RMP generated grooves but stationary jets dispensing three times the power of the 20 RPM generated grooves were of comparable depths to the 20 RPM grooves.

A first look at the effect of having greater confining pressure of 25 MPa suggests a potentially significant decrease in volume of material removed compared with the 20 MPa case. The modelling tool has great potential to investigate jetting at realistic and anisotropic stress states for hole depths of 4 to 5 km targeting geothermal resources.

References

1. Xiang, J., et al., *Numerical simulation of rock erosion performance of a high-speed water jet using an immersed-body method.* International Journal of Rock Mechanics and Mining Sciences, 2022. **158**: p. 105179.
2. Latham, J., et al. *Experimental and numerical investigation of high-pressure jetting fluids impinging on submerged hard rock under deep geothermal downhole drilling conditions*. in *European Geothermal Congress 2022*. 2022.
3. Munjiza, A., *The combined finite-discrete element method*. 2004: John Wiley & Sons.

4. Xiang, J., A. Munjiza, and J.P. Latham, *Finite strain, finite rotation quadratic tetrahedral element for the combined finite–discrete element method.* International journal for numerical methods in engineering, 2009. **79**(8): p. 946-978.
5. Lei, Q., et al., *Effects of geomechanical changes on the validity of a discrete fracture network representation of a realistic two-dimensional fractured rock.* International Journal of Rock Mechanics and Mining Sciences, 2014. **70**: p. 507-523.
6. Mahabadi, O.K., et al., *Y-Geo: new combined finite-discrete element numerical code for geomechanical applications.* International Journal of Geomechanics, 2012. **12**(6): p. 676-688.
7. Latham, J.-P., et al., *Numerical modelling of forces, stresses and breakages of concrete armour units.* Coastal Engineering Proceedings, 2014. **1**(34): p. 78.
8. Guo, L., et al., *A numerical investigation of mesh sensitivity for a new three-dimensional fracture model within the combined finite-discrete element method.* Engineering Fracture Mechanics, 2016. **151**: p. 70-91.
9. Munjiza, A., D.R.J. Owen, and N. Bicanic, *A combined finite-discrete element method in transient dynamics of fracturing solids.* Engineering Computations, 1995. **12**(2): p. 145-174.
10. Tatone, B.S.A. and G. Grasselli, *A calibration procedure for two-dimensional laboratory-scale hybrid finite–discrete element simulations.* International Journal of Rock Mechanics and Mining Sciences, 2015. **75**: p. 56-72.
11. Lisjak, A., et al., *Acceleration of a 2D/3D finite-discrete element code for geomechanical simulations using General Purpose GPU computing.* Computers and Geotechnics, 2018. **100**: p. 84-96.
12. Munjiza, A. and K. Andrews, *Penalty function method for combined finite–discrete element systems comprising large number of separate bodies.* International Journal for numerical methods in engineering, 2000. **49**(11): p. 1377-1396.
13. Dehkhoda, S. and M. Hood, *An experimental study of surface and sub-surface damage in pulsed water-jet breakage of rocks.* International Journal of Rock Mechanics and Mining Sciences, 2013. **63**: p. 138-147.